Comparison of Airborne In Situ, Airborne Radar–Lidar, and Spaceborne Radar–Lidar Retrievals of Polar Ice Cloud Properties Sampled during the POLARCAT Campaign

JULIEN DELANOË,* ALAIN PROTAT,+ OLIVIER JOURDAN,# JACQUES PELON,@ MATHIEU PAPAZZONI,@ RÉGIS DUPUY,# JEAN-FRANCOIS GAYET,# AND CAROLINE JOUAN@

* *Laboratoire Atmosphère, Milieux, et Observations Spatiales, Guyancourt, France*
+ *Centre for Australian and Weather and Climate Research, Melbourne, Victoria, Australia*
# *Laboratoire de Météorologie Physique, Université Blaise Pascal/CNRS/OPGC, Aubiére, France*
@ *Laboratoire Atmosphère, Milieux, et Observations Spatiales, Jussieu, France*

(Manuscript received 14 November 2011, in final form 3 August 2012)

ABSTRACT

This study illustrates the high potential of RALI, the French airborne radar–lidar instrument, for studying cloud processes and evaluating satellite products when satellite overpasses are available. For an Arctic nimbostratus ice cloud collected on 1 April 2008 during the Polar Study using Aircraft, Remote Sensing, Surface Measurements and Models, of Climate, Chemistry, Aerosols, and Transport (POLARCAT) campaign, the capability of this synergistic instrument to retrieve cloud properties and to characterize the cloud phase at scales smaller than a kilometer, which is crucial for cloud process analysis, is demonstrated. A variational approach, which combines radar and lidar, is used to retrieve the ice-water content (IWC), extinction, and effective radius. The combination of radar and lidar is shown to provide better retrievals than do stand-alone methods and, in general, the radar overestimates and the lidar underestimates IWC. As the sampled ice cloud was simultaneously observed by *CloudSat* and *Cloud–Aerosol Lidar and Infrared Pathfinder Satellite Observations* (*CALIPSO*) satellites, a new way to assess satellite cloud products by combining in situ and active remote sensing measurements is identified. It was then possible to compare RALI to three satellite ice cloud products: *CloudSat*, *CALIPSO*, and the Cloud-Aerosol-Water-Radiation Interactions (ICARE) center's radar–lidar project (DARDAR).

1. Introduction

Spaceborne radar and lidar on board *CloudSat* (Stephens et al. 2002) and the *Cloud Aerosol lidar and Infrared Pathfinder Satellite Observations* (*CALIPSO*; Winker et al. 2003) satellite present us with an amazing opportunity to tackle questions about the influence of clouds in forecasts and climate predictions at global scale (Waliser et al. 2009; Delanoë et al. 2011). The combination of spaceborne radar and lidar remains the most accurate technique for documenting vertical cloud properties at global scale (Mace et al. 2009; Delanoë and Hogan 2010; Stein et al. 2011). However, both instruments reach their limit when local cloud processes need to be investigated as the radar–lidar footprint exceeds 1 km along track. Ground-based radar–lidar instruments are perfectly designed for long-term observations (Illingworth et al. 2007; Bouniol et al. 2010) at high temporal resolution but are limited to very local measurements and it is therefore difficult to study clouds over oceans, for instance. To close the gap between the global (satellites) and local (ground-based station) scales, airborne platforms can be deployed. Such platforms have many advantages: among them is the possibility to characterize cloud properties at very fine scales while linking them to the regional scale. Airborne radar–lidar instruments are also very useful for evaluating satellite products when the aircraft takes concurrent in situ measurements under a satellite track (Deng et al. 2010; Mioche et al. 2010) and can also be used to evaluate instrument calibration, as shown in Protat et al. (2011a).

In this paper we investigate an Arctic nimbostratus ice cloud sampled by the airborne radar–lidar platform (RALI; Protat et al. 2004) developed at the Institut

Corresponding author address: Julien Delanoë, Laboratoire Atmosphère, Milieux, et Observations Spatiales (LATMOS), IPSL/UVSQ/CNRS, Boulevard D'Alembert, Guyancourt 78280, France.
E-mail: julien.delanoe@latmos.ipsl.fr

DOI: 10.1175/JTECH-D-11-00200.1

Pierre Simon Laplace (IPSL) and Laboratoire Atmosphère, Milieux, et Observations Spatiales (LATMOS) during the Polar Study using Aircraft, Remote Sensing, Surface Measurements and Models of Climate, Chemistry, Aerosols, and Transport (POLARCAT; see the special issue on POLARCAT in *Atmos. Chem. Phys.*) spring campaign, which took place in the north of Sweden during 2008. The general aim of the POLARCAT campaign was to identify the impact of trace gases, aerosols, and heavy metals, which are transported to the Arctic and their impact on climate in the Arctic region. This campaign involved numerous research institutes in a joint effort to collect a large dataset of measurements (aircraft, balloons, ground-based sensors, and satellites) and perform modeling studies. The primary aim of this study is to evaluate the RALI retrieval using in situ measurements at the location closest to the aircraft altitude. A secondary objective is to use the RALI measurements to evaluate satellite cloud products at regional scale. In section 2, the context of the study and the RALI configuration are described. The retrieval technique and a comparison with in situ measurements are presented in section 3. The RALI ice cloud retrievals are then used to evaluate *CloudSat* and *CALIPSO* products in section 4.

2. Description of RALI experimental campaign

a. The RALI platform

The idea of combining radar and lidar measurements and exploiting the many advantages/benefits of their synergy for cloud studies originated in the early 1990s with Intrieri et al. (1993), and this combination has already been used to study Arctic clouds (Intrieri et al. 2002; Shupe et al. 2006; Eloranta et al. 2007).

Due to their wavelengths, radar and lidar are sensitive in different ways to the same hydrometeors. Lidar measurements are directly linked to extinction, which can be considered proportional to the second moment of the particle size distribution if we assume spherical ice particles. As a result, lidar signal is strongly dominated by the concentration of the hydrometeors. In contrast, the radar has a lower frequency and in Rayleigh approximations the radar reflectivity is proportional to the sixth moment of the particle size distribution, which makes the radar measurement very dependent on the particle size. Practically, these different characteristics have many advantages.

By combining both instruments to simultaneously detect a valid signal over the same region (hereinafter defined as the overlap region), one can retrieve particle size and concentration. The difference in sensitivity can also be a strength; the lidar is more sensitive to small liquid drops or small crystals while the radar is more sensitive to large crystals. The lidar can detect thin clouds composed of both ice crystals and liquid droplets that are not detectable by the radar, but the radar measurement can deeply penetrate ice clouds when the lidar signal is extinguished. RALI consists of a combination of the 95-GHz Doppler Radar System Airborne (RASTA) and the Leandre New Generation (LNG) lidar, both of which are nadir pointing. LNG was in its backscatter configuration, operating at three wavelengths (355, 532, and 1064 nm), including depolarization at 355 nm. The main characteristics of RALI instruments are summarized in Table 1.

TABLE 1. RALI characteristics.

RALI	RASTA (radar)	LNG (lidar)
Wavelength (frequency)	3.2 mm (95.04 GHz)	355/532/1064 nm
Vertical resolution (m)	60	7.5 averaged to 60
Range (km)	15	15
Integration time (ms)	250	50 (minimum)
Energy	1.6 kW	60/10/80 mJ
Ambiguous velocity (m s^{-1})	8	—
Full-angle beamwidth (mrad)	—	0.16/4/6.5
Sensitivity	$\simeq -40$ dBZ at 1 km	Molecular scattering
ATR-42 speed (m s^{-1})	$\simeq 100$	

Since 2010 the LNG lidar has had a high spectral resolution capability added at 355 nm. Unfortunately, the high spectral resolution capability was not operational during the POLARCAT campaign. Both instruments were on board the French ATR-42 aircraft. In situ measurements were also available on board the ATR-42 to characterize ice cloud microphysical properties at finescale (i.e., the sampling volume is about 1 L). Total ice concentration, particle habit, scattering phase function, and particle size distribution were measured using a cloud particle imager (CPI; Lawson et al. 2001), two-dimensional optical array probes (2DC–2DP), and a polar nephelometer (PN; Gayet et al. 2002a). The main characteristics of the in situ probes are provided in Table 2.

b. Meteorological context

There were 12 ATR-42 flights between 30 March and 11 April 2008 where RALI was operated. In this paper we focus on one specific case collected during 1 April 2008, north of Kiruna, Sweden, when the ATR-42 took off at 0920 UTC to sample the area above northern Norway and the Arctic Ocean for 3 h, 45 min. This case

TABLE 2. Characteristics of the in situ probes used in the study.

Probes	Diameter range (μm)	References
2D cloud probe (2DC)	25–800	Knollenberg (1970); Strapp et al. (2001)
2D precipitation probe (2DP)	200–6400	Knollenberg (1970)
Cloud Particle Imager (CPI)	10–2000	Lawson et al. (2001)
Polar nephelometer (PN)	3–800	Gayet et al. (2002b)

study has been chosen for its combination of cirriform parts and precipitating area, showing simultaneously thin and very thick ice clouds to highlight the radar–lidar complementarity, and because it was the only one to coincide with a satellite overpass.

The general meteorological situation at 1100 UTC is represented in Fig. 1 by a visible image of the Moderate Resolution Imaging Spectroradiometer (MODIS), where the flight track is shown in red. As shown by the radar reflectivity from RASTA and attenuated backscatter at 532 nm from LNG in Figs. 2a and 2b, respectively, a moderately thick ice cloud is present with a precipitating part spanning from 69.5° to 70.5°N (corresponding to 1000–1100 UTC). Note that the RASTA radar was calibrated using the technique of Li et al. (2001) and Protat et al. (2011a) and showed that the error in calibration was less than 1 dBZ. RASTA sensitivity was estimated at around −35 dBZ at 1 km (Protat et al. 2011a). Figure 1c exhibits a merged mask created using both radar and lidar measurements following the same technique as that used in Delanoë and Hogan (2010). In this very cold region most of the cloud is made of ice but we clearly notice supercooled layers spanning along the aircraft trajectory.

These supercooled layers occur at the top of the lowest cloud level, an observation that corroborates the findings of Rauber and Tokay (1991). They explained the existence of supercooled water at the top of cold clouds by "the imbalance between the condensate supply rate and the bulk ice crystal mass growth rate at wide range of temperatures and updraft speeds." Supercooled layers are identified using the strong lidar return signal due to the high concentration of small droplets while the radar sensitivity does not allow us to see these layers. However, it is not possible to determine if there are any supercooled layers below the area where the lidar is completely extinguished as the radar cannot observe such small droplets. Mixed-phase clouds are commonly observed at these high latitudes. Yoshida et al. (2010) showed that, for the polar region, the fraction of liquid water below the freezing level and below 3 km was about 8% using satellite radar and lidar data. These mixed-phase layers play an important role in the radiative budget in the Arctic due to their longevity and their

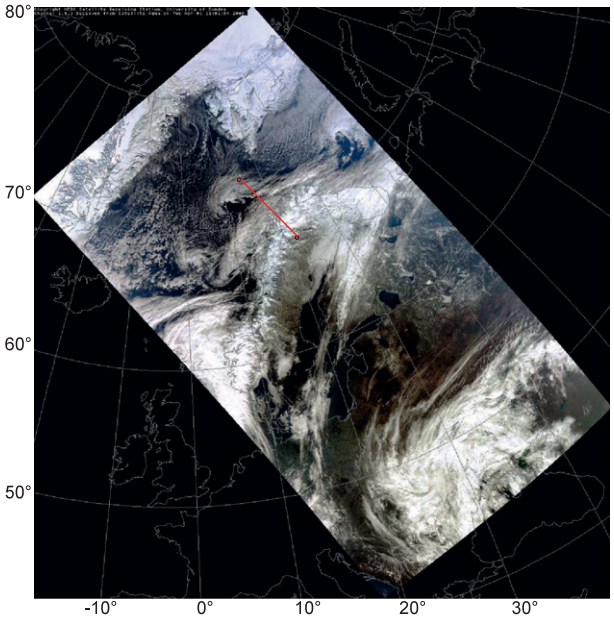

FIG. 1. MODIS visible image above Sweden at 1100 UTC 1 Apr 2008. The flight track corresponding to the study is represented in red.

characteristics (Shupe and Intrieri 2004; de Boer et al. 2009; Shupe et al. 2011; Shupe 2011).

3. Cloud properties from RALI

a. Radar–lidar algorithm

As mentioned in the previous section, radar and lidar can be used to retrieve cloud properties. This combination was initiated by Intrieri et al. (1993) but the technique was limited to very optically thin clouds as the lidar attenuation was neglected. Later on, Wang and Sassen (2002), Okamoto et al. (2003), and Tinel et al. (2005) used the radar signal to correct the lidar attenuation. Mitrescu et al. (2005) were one of the first to propose the variational approach to retrieve ice cloud properties from radar–lidar combinations; however, only the overlap region was used to retrieve cloud properties.

In this study we use the variational synergistic algorithm (Varcloud) developed by Delanoë and Hogan (2008). This algorithm retrieves ice cloud properties [visible extinction, ice-water content (IWC), and effective radius (Re)] seamlessly between regions of the cloud detected by both radar and lidar, and regions detected by just one of these two instruments. Typically, when the lidar signal is unavailable due to strong attenuation, the variational approach ensures that the retrieval tends toward similar values to those that would be obtained using an empirical relationship using the

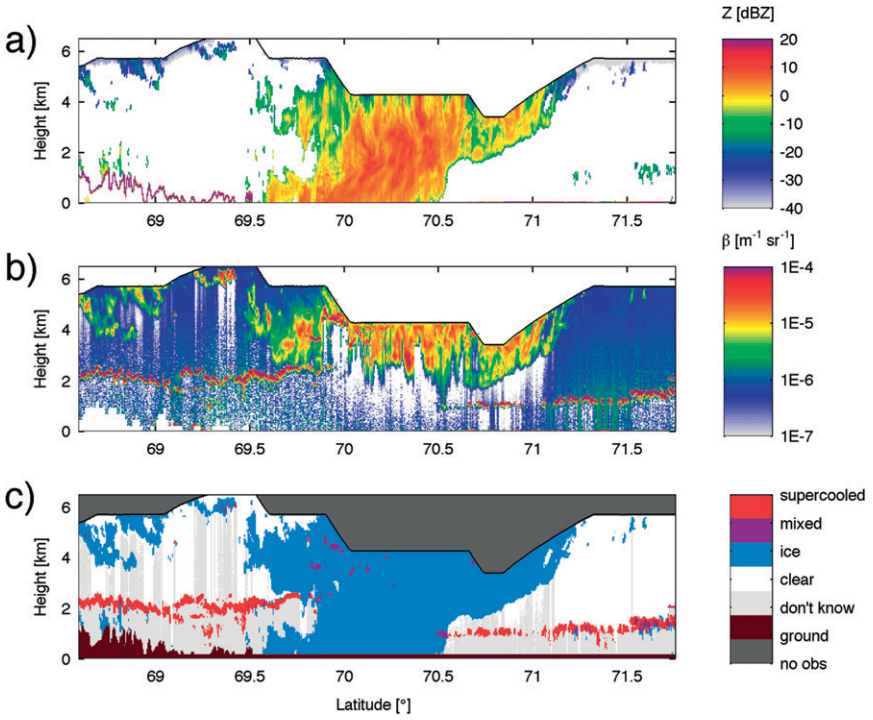

FIG. 2. Latitude–height representation of a polar cloud sampled on 1 Apr 2008 by the RALI instruments during the POLARCAT spring campaign. (a) RASTA radar reflectivity (Z), (b) LNG lidar attenuated backscatter (β), and (c) the merged mask derived from both instruments (see details in the text).

radar reflectivity factor and temperature (temperature can be obtained from model or aircraft measurements). On the other hand, when the radar is not sensitive enough to detect the cloud, the retrieved extinction is converted to IWC using lookup tables. Details of the method can be found in Delanoë and Hogan (2008, 2010). The retrieval technique uses the optimal estimation framework and the Gauss–Newton method (Rodgers 2000) to minimize iteratively the difference between the forward-modeled observations and real observations. This approach includes a rigorous treatment of measurements and forward model errors. At each step, forward-modeled radar reflectivity and lidar-attenuated backscatter are computed using the forward model and the state vector containing extinction, extinction-to-backscatter ratio, and number concentration. Once the convergence is achieved, the optimal state vector is converted to IWC and Re using lookup tables. Note that in the case of nonconvergence, the cloud properties profile is not retrieved. The forward model assumes a microphysical model describing the shape of the particle size distribution (PSD) using the normalized approach (Delanoë et al. 2005). In the standard version of the algorithm, the mass–size relationship used to derive the lookup table linking ice cloud properties to measurement parameters follows a power law proposed by Brown and Francis (1995) for spherical aggregates, which can be applied to many kinds of ice clouds (Heymsfield et al. 2010). The corresponding area–size relationship is taken from Francis et al. (1998), who used the same aircraft dataset as Brown and Francis (1995). However, it is possible to change the particle habits for specific studies. For instance, in section 3c, we also retrieve cloud properties using the rimed dendrites relationship assumption. The sensitivity of the algorithm to the mass size relationship using satellite data can be found in Stein et al. (2011). The lidar forward model accounts for multiple scattering and attenuation using the model of Hogan (2006).

b. *RALI retrieval*

The method previously described is applied to the RALI measurements. The RASTA radar reflectivity and LNG lidar attenuated backscatter at 532 nm are assimilated to retrieve ice cloud properties. The lidar signal below and in the supercooled layers is not assimilated in the retrieval and therefore the radar takes over in these areas. Resulting IWC (IWC_{RALI}), visible extinction, and Re (using standard mass–size assumption) are presented in Figs. 3a–c, respectively. It clearly

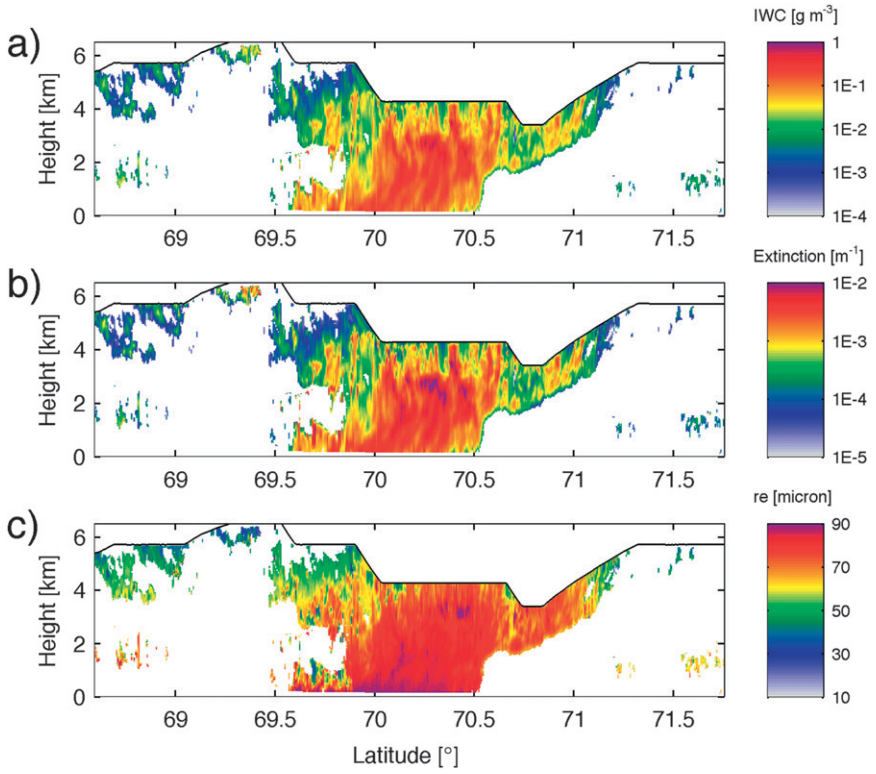

FIG. 3. Latitude–height representation of the synergistic radar–lidar retrieval of ice cloud properties, (a) IWC, (b) visible extinction, and (c) effective radius (Re), for 1 Apr 2008 during the POLARCAT spring campaign.

appears that cloud properties are retrieved seamlessly between regions of the cloud sampled by both radar and lidar and regions detected by just one of these two instruments. Any part of the ice cloud can be retrieved from the thin ice part before 69.5°N to the precipitating core between 69.5° and 70.5°N. RALI retrieval can be used for cloud process studies, for instance in the precipitating region below 3-km effective radius, increasing and potentially highlighting the aggregation process. This hypothesis of aggregation is corroborated by Fig. 4, where the number concentration and effective radius, averaged between latitudes 70° and 70.5°, are represented. Below 2.7 km, N_t is decreasing while Re is decreasing with height. The right-hand panel in Fig. 4 shows the average value of Doppler velocity, which indicates that the ice particles velocity increases due to the increase in their size. Note that the increase in velocity is not monotonic, which can be explained by the fact that Doppler velocity corresponds to the contribution of the terminal fall velocity of ice particles and vertical air motion.

c. *RALI retrieval and in situ measurements*

The retrieved IWC and visible extinction are compared to in situ measurements available on board the same aircraft, such as CPI, 2DC and 2DP probes, and the polar nephelometer. Unfortunately, no bulk measurement of IWC was available, but two different methods have been used to calculate the ice-water content. The merged spectra of 2DC and 2DP have been used to compute IWC assuming a rimed dendrites mass–size relationship (hereafter $IWC_{2DC-2DP}$). The CPI images show that the shape of the observed ice particles is close to that of the rimed dendrite for the period under examination. The second approach for deriving IWC (hereafter IWC_{CPI}) exploits the combination of the CPI particle size distribution and the particle shape analysis (Mioche et al. 2010). This combination allows us to use the best corresponding mass–size relationship from the literature for each recognized habit and obtain an optimal IWC (Lawson and Baker 2006; Protat et al. 2011b). The comparison has been carried out using two different RALI retrievals: one retrieval using the standard mass–size relationship from Brown and Francis (1995) and the other one using the rimed dendrites assumption.

The results of the comparison are shown in Fig. 5, where panel (a) represents the binned latitude IWC retrieved from in situ and RALI measurements at the two closest valid radar and/or lidar gates to the aircraft

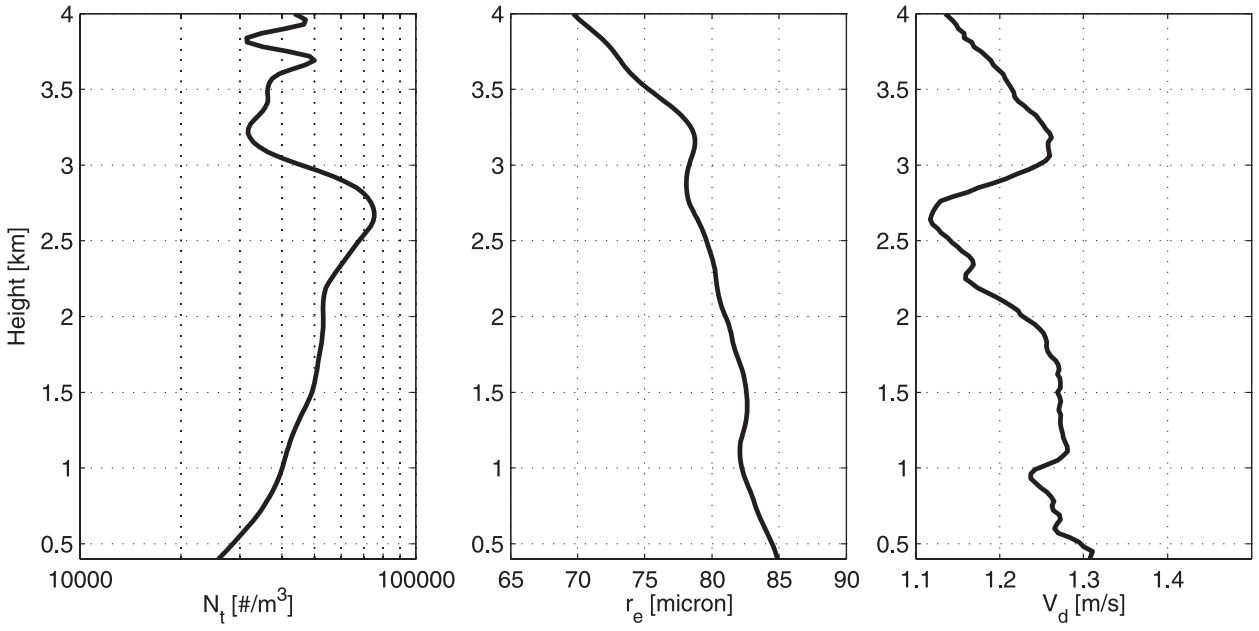

FIG. 4. Averaged values of number concentration N_t, effective radius Re, and Doppler velocity V_d as a function of height corresponding to the precipitating core between latitudes 70° and 70.5°.

(on average less than 150 m). IWC is linearly averaged along the aircraft track in bins of 0.01° of latitude where the associated in situ temperatures vary from −47° to −19°C. The first striking result is the good agreement, in terms of variation as a function of the latitude and order of magnitude, between the in situ measurements and the remote sensing retrieval despite the heterogeneity of the vertical cloud structure. It is obvious that the remote sensing measurements are not taken exactly at the same location as the in situ probes and the sampled volume is much larger (e.g., the radar gate size is 60 m). RALI reproduces the variations as a function of latitude seen in the in situ measurements. In the latitude interval (70.15°–72°N), IWC_{RALI} and in situ results are in good agreement, except at a few areas, around 70.4°, 70.9°, and 71.05°N, where RALI underestimates both IWC_{CPI} and $IWC_{2DC-2DP}$. Figure 5b shows the averaged relative difference between IWC_{CPI} and the other IWC values (i.e., $(IWC_{CPI} - IWC)/IWC_{CPI}$): RALI using the spherical aggregates or rimed dendrites assumptions and $IWC_{2DC-2DP}$. The relative difference, given as a function of IWC_{CPI}, corroborates the relative good agreement between RALI and in situ measurements between 0.01 and 0.08 g m^{-3}, where values remains within the −60% to 60% interval and are less than 20% at 0.01 and 0.025 g m^{-3}. It is also important to note that the differences between in situ probes, and between in situ probes and RALI, are quite similar above 0.01 g m^{-3}. From these graphics, it is clear that RALI IWC retrieval is not very sensitive to the two mass–size relationship assumptions tested in this study, and this is especially true above 0.01 g m^{-3}. In general, RALI retrievals seem to overestimate IWC below 0.01 g m^{-3}, except around 0.003 g m^{-3}; this result can be explained by the difference in the sampled volume, as the RALI sampled volume is larger than from in situ measurements. The same conclusion is reached when $IWC_{2DC-2DP}$ is used as reference (not shown here). The relative difference between the RALI and in situ results can reach high values at a given IWC, but when we calculate the total mean relative differences, they correspond to about 23% and 7% for the 2DC–2DP and CPI, respectively, due to compensating effects and domination of high content. Figure 5b also shows an important discrepancy between IWC_{CPI} and $IWC_{2DC-2DP}$ for low values, this can be explained by the fact that the CPI measurement errors for characterizing the particle size distribution are generally larger than for the 2D probes due to a smaller sampling volume than 2DP. Despite a longer time integration, the CPI is still penalized for measuring small values of IWC. However, the CPI errors on the size distribution and derived microphysical parameters are expected to be of the same order as those obtained with the PMS 2DC or 2DP instruments: up to 75% on the particle concentration and 100% on the IWC (Gayet et al. 2002b). This result is explained by the fact that the CPI allows one to retrieve better IWC for the large value as it uses the particle shape analysis to adjust the mass–size relationship. This is the reason why IWC_{CPI} is used as reference here.

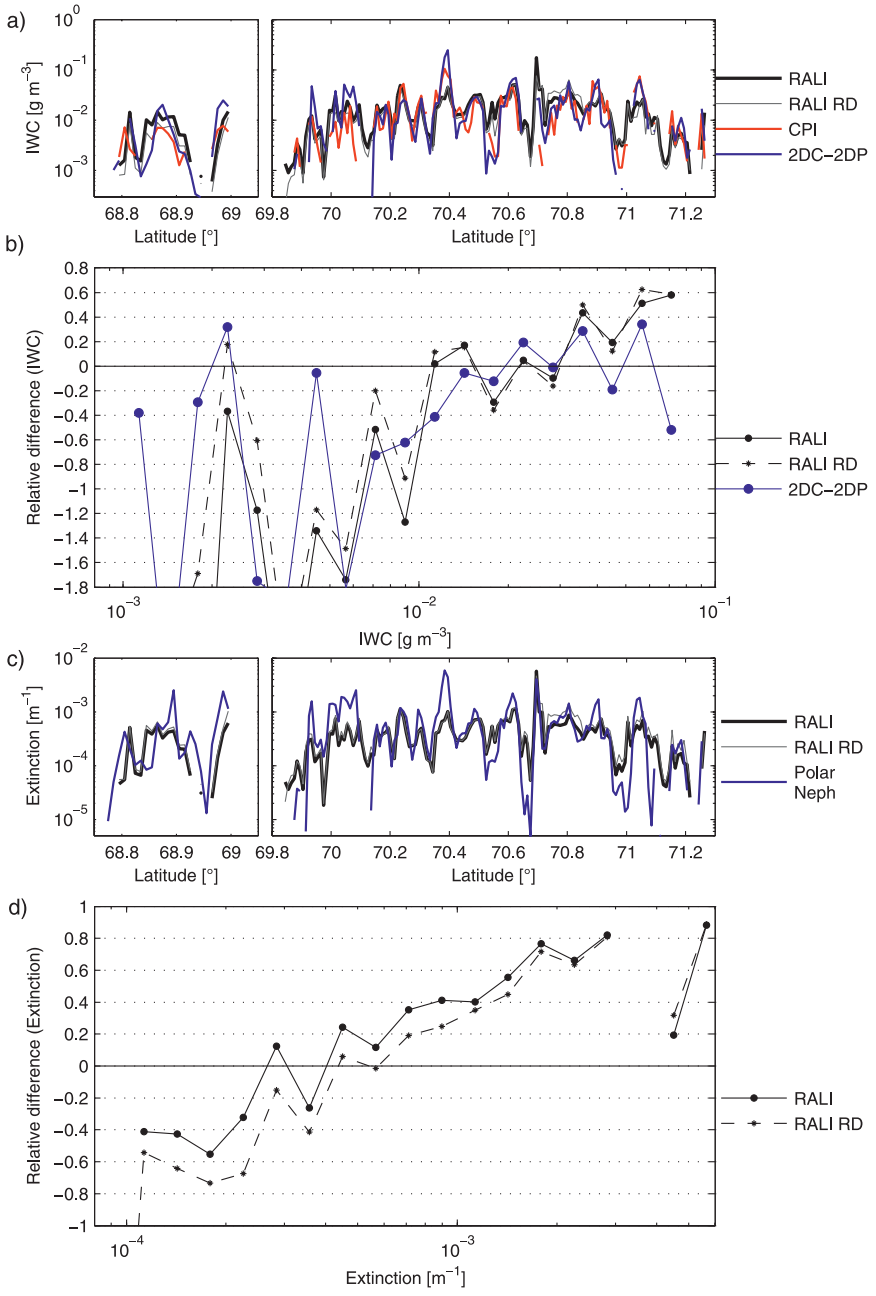

FIG. 5. Illustration of the comparison between the RALI retrievals and the in situ measurements. (a) IWC derived from CPI and 2DC–2DP probes, RALI with the spherical aggregates assumption, and rimed dendrites (RD) as a function of latitude. (b) The relative difference between IWC (CPI) and IWC (2DC–2DP), standard RALI, and RALI (RD) retrievals as a function of IWC (CPI). (c) The extinction derived from the PN and RALI for the standard and rimed dendrites mass–size relationships as a function of latitude. (d) The relative difference in extinction as a function of PN extinction.

A comparison between PN and RALI extinctions is also presented in Fig. 5c. Some of the previous remarks regarding IWC are still valid for extinction. For example, RALI reproduces the variations as a function of latitude seen in the in situ measurements but with less variability. This is obvious between 69.8° and 70.1°N and at 70.4°N. Figure 5d shows the relative difference between the PN and RALI extinctions as a function of PN

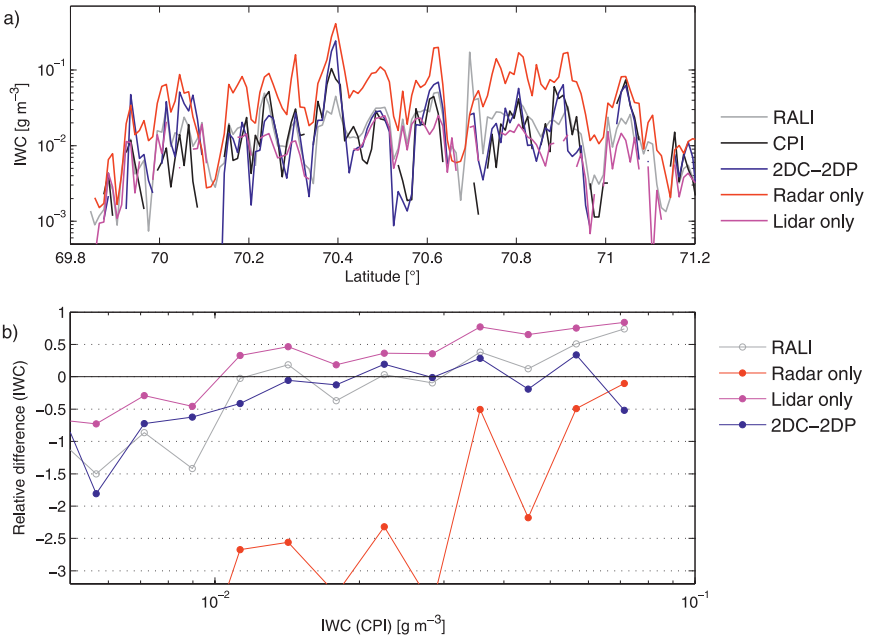

FIG. 6. Illustration of the impact of coupling radar and lidar in airborne IWC retrievals. (a) IWC values as a function of latitude. (b) The relative difference in IWC as a function of IWC measured by CPI.

extinction. The RALI-retrieved extinction is quite insensitive to the mass–size assumption above 8×10^{-3} m^{-1} and the rimed dendrites assumption seems to reduce the relative difference for extinction greater than 4×10^{-4} m^{-1} compared to Brown and Francis (1995). From Fig. 5d we can see that RALI retrievals overestimate extinction below 4×10^{-4} m^{-1} and underestimate above this value but remain within the −80% to 80% interval. The best results are obtained for the $2.5–8 \times 10^{-4}$ m^{-1} range with less than 40%. Note that the mean relative difference exceeds the error in PN measurements of 25% (Gayet et al. 2002a). A potential explanation for the discrepancy between PN and RALI extinctions could be the presence of liquid droplets. In a few regions, even the lidar may not detect very low concentrations of liquid water due to the volume sampling, while the PN can. This hypothesis is confirmed when relative differences in extinction are plotted against the liquid water content retrieved using the forward scattering spectrometer probes (FSSP) (not shown). Relative difference tends to increase as the LWC increases; this is especially true when LWC exceeds 10^{-2} g m^{-3}. Note that when the liquid droplets dominate the mixture (i.e., for large LWC), the lidar and PN are expected to yield similar results.

The presence of liquid droplets is probably not the only reason why large IWC and extinction appear to be underestimated by RALI, and independently from the mass–size assumptions. The differences between in situ measurements and remote sensing retrievals in these areas could be due to shattering effects (Korolev and Isaac 2005; Field et al. 2006; Heymsfield 2007), when large ice crystals are shattered on probes with shrouded inlets such as CPI, 2DC, and PN. As a result, the ice concentration for small particles artificially increases, which leads to overestimations in extinction and IWC. If we consider that large values of IWC and extinction correspond to sampled volumes containing large particles, it would explain some of the differences observed in Fig. 5 for large IWC.

We can also investigate the impact of using the radar–lidar synergy instead of using single-instrument retrievals; the potential of the radar–lidar combination is obvious, as mentioned previously, but it remains to quantify the contribution of each instrument. The retrieval technique of Delanoë and Hogan (2008) does not work only in the radar–lidar overlap, but can also retrieve IWC using only one of the instruments. Since only one unique moment of the PSD can be retrieved, the other relies on a priori information. As a priori information, we use a relationship between the number concentration and the extinction, which depends on temperature. This relationship was built using an extensive database including field campaigns of in situ measurements all over the globe. The radar- and lidar-only retrievals of IWC are compared with the in situ measurements and the radar–lidar retrieval in Fig. 6. All retrievals were obtained with the mass–size relationship corresponding

to spherical aggregates (i.e., Brown and Francis 1995). Relative differences in IWC as a function of IWC_{CPI} are represented in Fig. 6b. It is obvious that the radar-only retrieval largely overestimates the retrieved IWC by more than 200% below 3×10^{-2} g m^{-3}. The lidar-only retrieval slightly underestimates IWC for values less than 10^{-2} g m^{-3}. When radar and lidar are combined, the relative difference is clearly reduced (less than 30% in absolute values between 10^{-2} and 4×10^{-2} g m^{-3}). Note that for this comparison only the data where radar and lidar measurements were available have been used, explaining the differences with Fig. 5b. This striking example shows the advantage of combining radar and lidar instruments. The radar reflectivity is dominated by the large particles, and the lidar signal by the concentration. Therefore, the combination allows one to retrieve two moments of the particle size distribution and an optimal IWC. This is verified by the fact that the lidar-only retrieval is slightly better for values of IWC below 8×10^{-3} g m^{-3}, and radar-only retrieval gives satisfactory results for the largest values of IWC. Single-instrument retrieval techniques convert extinction or Z in IWC using statistical relationships. As mentioned above, extinction is a lower moment of the PSD than IWC while Z is a higher moment. Therefore, the IWC–Z relationship is dominated by large particles and the IWC–extinction connection is dominated by small particles. When radar and lidar are used together, the balance between small and large particle contributions is maintained. The reason why IWC does not increase when we add lidar information is that both relationships are used simultaneously in the retrieval.

4. Using RALI to evaluate satellite products

a. Airborne and satellite measurement collocation

In the previous section we compare the RALI retrievals with the in situ measurements at the location closest to the aircraft. In this section we want to evaluate two official products from *CloudSat* and *CALIPSO*, and the DARDAR synergistic radar–lidar product derived from *CloudSat* and *CALIPSO* measurements. The common approach is to collocate satellite products and in situ measurements (Deng et al. 2010; Mioche et al. 2010). Unfortunately, it is a fastidious task since the collocation can be a source of important errors. For instance, satellite and airborne tracks can be reasonably collocated but the satellite observation is an instantaneous picture of the meteorological situation and since the airborne sampling time is considerably longer, the meteorological situation may have changed. Furthermore, the comparison is made at a given altitude and it is impossible to analyze cloud property profiles. Accordingly, we suggest that a comparison of the satellite products is made not only with the in situ measurements but also with the airborne radar–lidar measurements to analyze the averaged profiles of cloud properties.

The case of 1 April 2008 was also sampled by *CloudSat* and *CALIPSO* satellites. The distance between the projected tracks of the aircraft and satellites is about 25 km at 68.5°N and it decreases to less than 1 km at 69.5°N (i.e., about the *CloudSat* footprint). The time difference between the aircraft track and the satellite's track varies between 85 min at 68.5°N and 30 min at 71.5°N. Figure 7 shows the collocated measurements from both *CloudSat* and *CALIPSO* and RALI, including the aircraft altitude as a function of the latitude. The MODIS 1-km optical phase (King et al. 1998) is also shown in Fig. 7m to illustrate the meteorological context. The MODIS instrument is on board the *Aqua* satellite, which is part of the A-Train satellite constellation. The red line is the projected ATR-42 track and the black one represents the satellite track (note that we assume that *CloudSat* and *CALIPSO* measurements are perfectly collocated). The ATR-42 flew above land from 68.5° to 69.4°N, going through ice and liquid cloud regions according to the MODIS cloud-phase product. This is corroborated by the RALI cloud-phase mask (Fig. 2c) but also by the strong lidar return of the Cloud–Aerosol Lidar with Orthogonal Polarization (CALIOP; see Fig. 7d) at 3-km altitude highlighting a supercooled layer on top of an ice cloud. We also notice that the *CloudSat* radar (Fig. 7b) detects more clouds below 4 km. This could be explained by two reasons. The first is that the observation time and location are different and therefore *CloudSat* and RASTA are not sampling the same scene; this is especially true between 68.5° and 70°N. However, LNG and CALIOP lidars seem to observe the same liquid cloud at 3 km, which would suggest that the meteorological situation has not drastically changed (MODIS imagery supports this statement). The second plausible explanation comes from the radar sensitivity. The RASTA sensitivity is about −35 dBZ at 1 km while *CloudSat* sensitivity (Tanelli et al. 2008; Protat et al. 2009) is almost vertically constant at about −30 dBZ in the troposphere. The radar RASTA is less sensitive than *CloudSat* close to the ground and would explain the observed differences.

Before the evaluation of cloud products, we pursue the comparison between satellite and RALI measurements. The underlying idea is to determine whether the differences are due to the measurements from each platform or due to the cloud property retrieval techniques

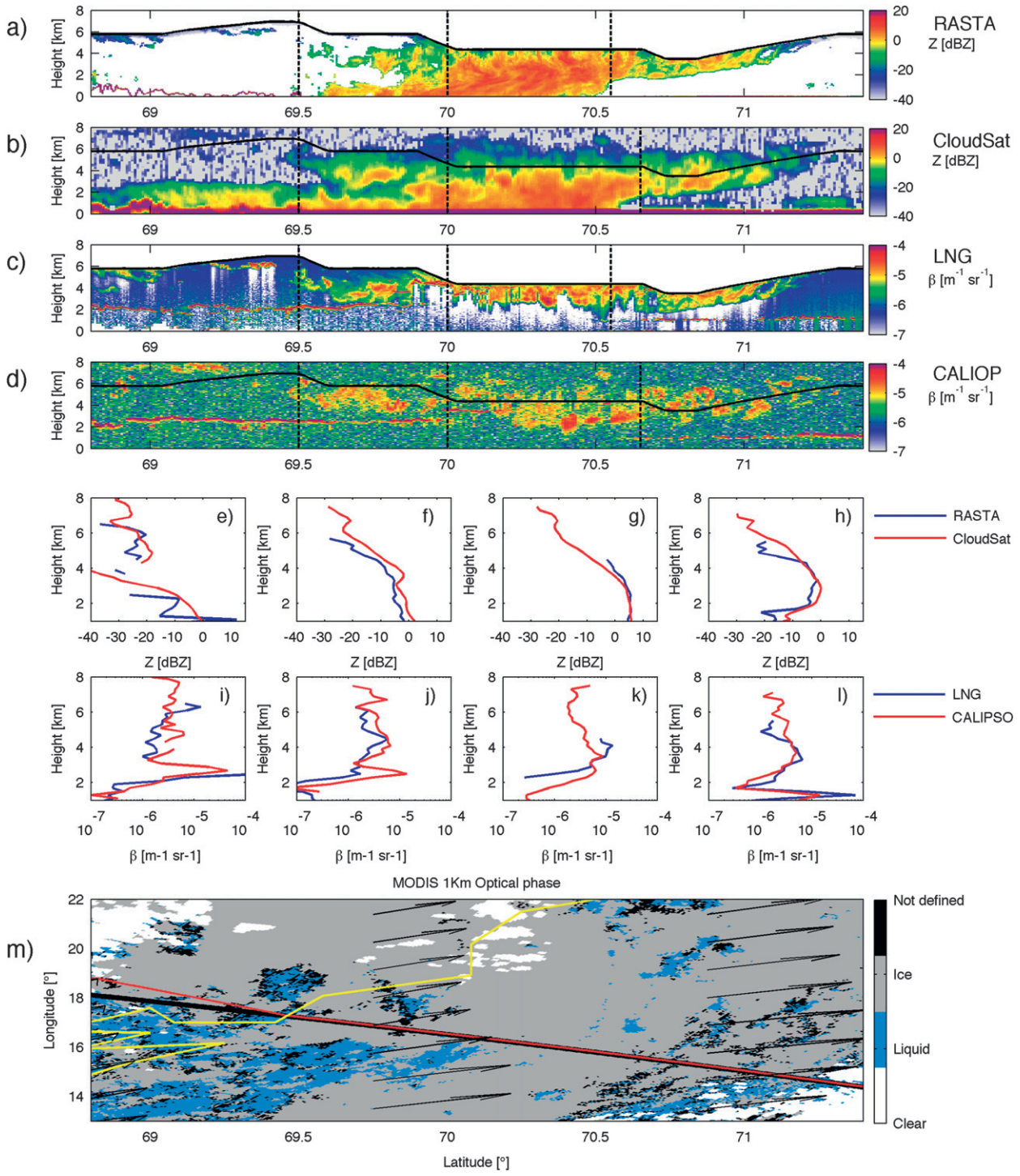

FIG. 7. Example illustration of the collocated RALI measurements from (a) RASTA, (c) LNG and the A-Train constellation, (b) *CloudSat*, (d) *CALIPSO*, and (m) the MODIS 1-km optical phase. In (a)–(d), the solid black line represents the aircraft altitude. The scene has been separated into four different regions (see text for details). For each region, the averaged values of reflectivity and backscatter coefficient have been calculated for each altitude bin and are represented in (e)–(l). Blue lines correspond to the RALI values, and red lines show the averaged values from *CloudSat* and *CALIPSO*, respectively. In (m), the red line shows the RALI aircraft track and the black line the satellite's track. Black arrows give an indication on the wind direction (from ECMWF reanalysis) at 5-km altitude and at the closest time to the observations. Yellow line indicates the coast of Sweden.

used. We need to assume that the meteorological situation has not completely changed if we want to compare both measurements and retrievals. Nevertheless, as shown in Fig. 7, the precipitation part of the ice cloud shows a slight shift toward high latitude between satellite and airborne measurements. This implies that we cannot directly compare profile-to-profile RALI and satellite measurements and, for this reason, we will base our comparison on four different latitude slices. The separations are visible in Fig. 7, where each latitude band is separated by vertical dotted lines. For each region, the averaged values of the reflectivity and backscatter coefficient have been calculated for each altitude bin and are represented in Figs. 7e–l. Blue lines correspond to the RALI values, while red lines show the averaged values for *CloudSat* and *CALIPSO*, respectively. First of all, we can see that the instruments are well calibrated and there is no obvious bias, despite a few differences. In the precipitating part between 70° and 70.8°N, the difference in reflectivity values is less than 1 dBZ. In the latitudes ranges from 69.5° to 70°N and for the part from the highest latitudes (Figs. 7f and 7h, respectively), the differences do not exceed 5 dBZ, except for the latter above 4.5 km. Note that in Fig. 7e that the reflectivity profile of RASTA is derived using a very small amount of data and therefore it cannot be compared to *CloudSat* values below 4 km. As shown in panels Fig. 7i–l, the differences in lidar backscatters are also reasonable (within ±50% relative difference) considering the fact that during daytime the CALIOP signal is noisier than the LNG signal.

b. Satellite product description

Since most of these products are already well documented in the literature we only give a short description below.

- DARDAR (for radar–lidar) is an operational *CloudSat–CALIPSO* product, available at the Cloud–Aerosol–Water–Radiation Interactions (ICARE) data center in France based on the method of Delanoë and Hogan (2010). The algorithm is very similar to the technique used for retrieving ice cloud properties from RALI. The main idea here is to use the RALI product to evaluate the satellite products. Note that the use of the same algorithm does not imply that the results will be identical since we are comparing very different instruments, scales, and viewing geometries. Retrieved properties are given at the *CloudSat* horizontal resolution (about 1.4 km) and 60-m vertical resolution.
- The level-2B radar-only cloud water content product (2B-CWC-RO), provided by the National Aeronautics and Space Administration (NASA) *CloudSat* project (Austin et al. 2009), is also included in the comparison. This product is the result of the assimilation of the *CloudSat* reflectivity and the model temperature from the European Centre for Medium-Range Weather Forecasts (ECMWF) to retrieve cloud water content. We limit our comparison to the ice part of the clouds. IWC is available at 1.4-km horizontal and 240-m vertical resolutions.
- The *CALIPSO* lidar level-2 cloud profile data at 5 km (V3–01 version; Young and Vaughan 2009) contain the cloud extinction at 532 nm and IWC with a horizontal spatial resolution of 5-km along track and 60-m vertical resolution. This retrieval uses the combination of the Hybrid Extinction Retrieval Algorithms (HERA; Young and Vaughan (2009), as well as scene classification and phase algorithms. The ice cloud water content, considered as the provisional product, is calculated using a parameterized function of the retrieved 532-nm extinction. The empirical relationship between extinction and IWC has been derived using an extensive in situ dataset (Heymsfield et al. 2005).

c. Results

We have already mentioned above that the collocation of satellite products and airborne measurements is a difficult task. Figure 8 depicts both IWC and extinction as a function of the latitude at the closest location to the aircraft and includes satellites products, RALI retrievals, and in situ measurements. *CloudSat* seems in general to overestimate IWC, by up to 150%, while *CALIPSO* tends to underestimate IWC by about 50%–100% (note that the $\mathrm{IWC}_{\mathrm{CALIPSO}}$ is smoother due to the 5-km horizontal resolution). This is an expected trend, which agrees with the results shown in Fig. 6 in section 3c. The DARDAR cloud product, combining radar and lidar measurements, seems to better match the in situ values (±50%). DARDAR and *CALIPSO* are in better agreement regarding the extinction retrieval. From this example it is obvious that in situ measurements cannot give a quantitative evaluation of the satellite products but they can give us an estimate of the order of magnitude expected for IWC and extinction retrievals. The strength of the RALI platform is to exploit the in situ measurements to evaluate or eventually constrain the radar–lidar retrieval; then the retrieval can be compared to satellite products. Even if it remains difficult to make profile-to-profile comparisons, we can statistically evaluate cloud properties profiles.

Figure 9 illustrates the comparison between each IWC product. From Figs. 9a–d we represent the *CloudSat* official IWC product ($\mathrm{IWC}_{\mathrm{CloudSat}}$), the 5-km IWC product from *CALIPSO* ($\mathrm{IWC}_{\mathrm{CALIPSO}}$), the DARDAR

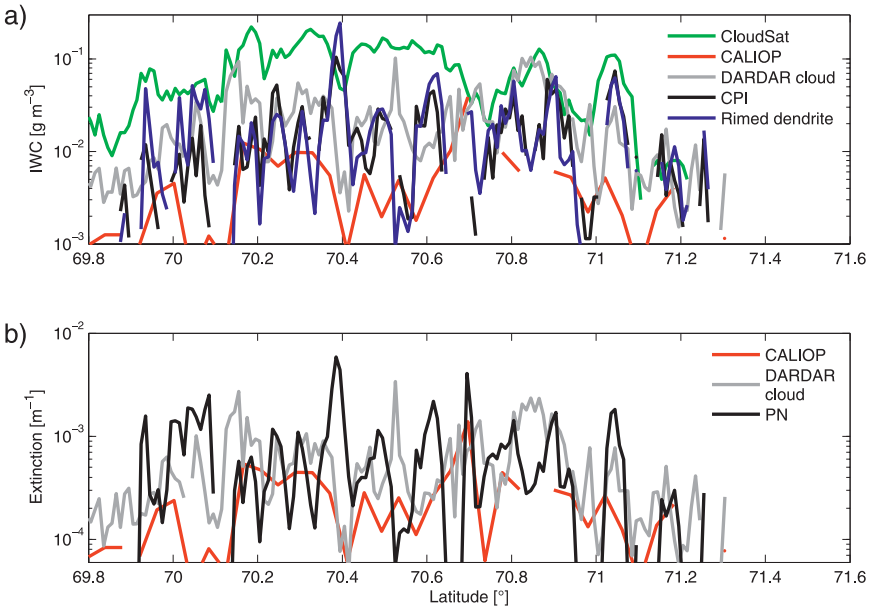

FIG. 8. As in Figs. 5a–d, but for official DARDAR, CALIOP, and *CloudSat* products.

IWC (IWC_{DARDAR}), and the RALI retrieval averaged over a 1-km footprint. The black horizontal line illustrates the aircraft altitude and the vertical dashed lines split the scene into several latitude regions, which will be analyzed in Figs. 9e–t. These panels show contour plots of the IWC distribution as a function of altitude, where each column corresponds to the latitude region delimited by the black dashed lines and each row corresponds to one product: Figure 9 also shows $IWC_{CloudSat}$ [panels (e–h)], $WC_{CALIPSO}$ [panels (i–l)], IWC_{DARDAR} [panels (m–p)], and IWC_{RALI} [panels (q–t)]. They all include mean profiles of IWC for each product, as well as a red line for *CloudSat*, a green line for *CALIPSO*, a magenta line for DARDAR, and a blue line for RALI. From these results we can see that in general $IWC_{CALIPSO}$ has the lowest values and $IWC_{CloudSat}$ the largest values and independently on the altitude. We also note that IWC_{DARDAR} lies mostly between the *CALIPSO* and *CloudSat* values, a result consistent with what we previously observed between single-radar and -lidar retrievals and synergistic retrieval. However, we observe a level of good agreement between the retrievals below 3 km, around 0.1 g m^{-3}, in the region starting at 70°N apart from *CALIPSO*, since the lidar is extinguished and the information is obtained mainly from the radar. Most of the time, DARDAR and RALI retrievals compare more favorably with each other than do the *CloudSat* and *CALIPSO* retrievals. This is expected since their retrieval techniques are identical and only the measurements are changing.

Figures 9e and 9m show that DARDAR and *CloudSat* are in good agreement around 2 km (about ±20%), but below 2 km, $IWC_{CloudSat}$ decreases while IWC_{DARDAR} increases as altitude decreases. This pattern of behavior has been highlighted by Stein et al. (2011). In the standard version of *CloudSat* retrieval, ice and liquid results are scaled linearly with temperature between 0° and −20°C by adjusting the respective particle number concentrations. This leads to a smooth transition to liquid-only retrievals at temperatures above 0°C. The Varcloud retrieval assumes that the radar reflectivity is dominated by the presence of ice particles and does not account for any liquid contribution below 0°C.

Figure 10 is equivalent to Fig. 9 for the visible extinction; however, only *CALIPSO*, DARDAR, and RALI are represented, since *CloudSat* cannot be used to accurately retrieve extinction. Contrary to what one might think, DARDAR, *CALIPSO*, and RALI extinction are in slightly better agreement than for IWC, although DARDAR extinction is slightly higher than the result retrieved by CALIOP. For example, in the latitude band between 70° and 70.5°N, the relative difference in extinction is between about 50% and 80% in IWC between DARDAR and *CALIPSO*. The lidar, by definition, measures the attenuated backscatter, which is strongly conditioned by the extinction. Therefore, the microphysical assumptions are limited to the way we treat multiple scattering and the extinction-to-backscatter ratio. In the *CALIPSO* retrieval technique, multiple scattering is corrected using a fixed correcting factor and

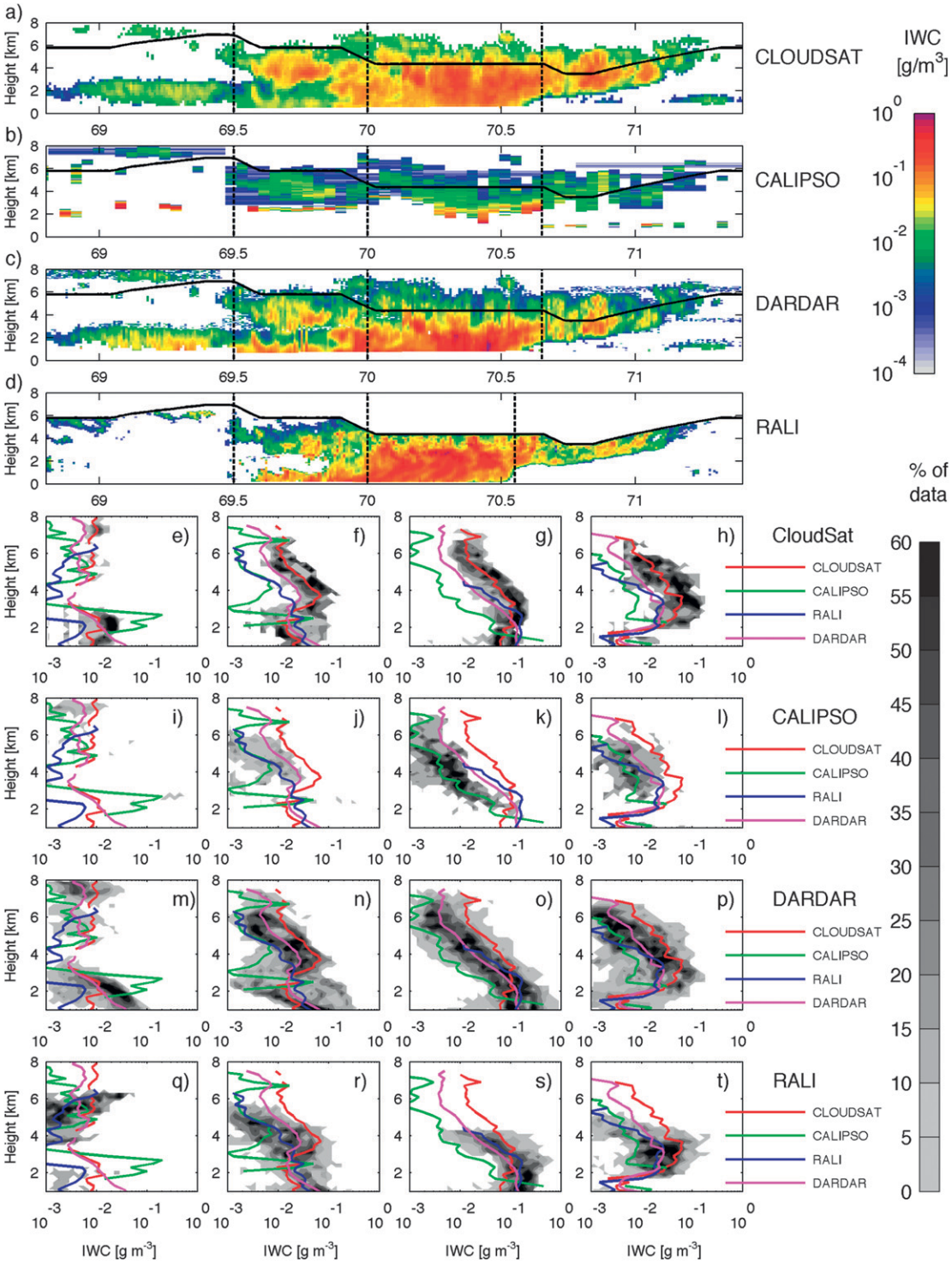

FIG. 9. Comparison between IWC retrieved from RALI, *CloudSat*, *CALIPSO*, and DARDAR products for 1 Apr 2008 during the POLARCAT spring campaign. (a)–(d) The latitude height IWC results from *CloudSat*, *CALIPSO*, DARDAR, and RALI, respectively. Aircraft altitude is visualized by the black thick line. The scene has been split into the same four different regions as in Fig. 7. For each region, the density distribution plots of IWC vs height are shown for (e)–(h) *CloudSat*, (i)–(l) CALIOP, (m)–(p) DARDAR, and (q)–(t) RALI. Pink lines represent the averaged values of DARDAR $\log_{10}$(IWC) for each altitude bin, and blue lines correspond to the RALI values. Red and green lines show the averaged values of IWC for the official product from both *CloudSat* and *CALIPSO*, respectively.

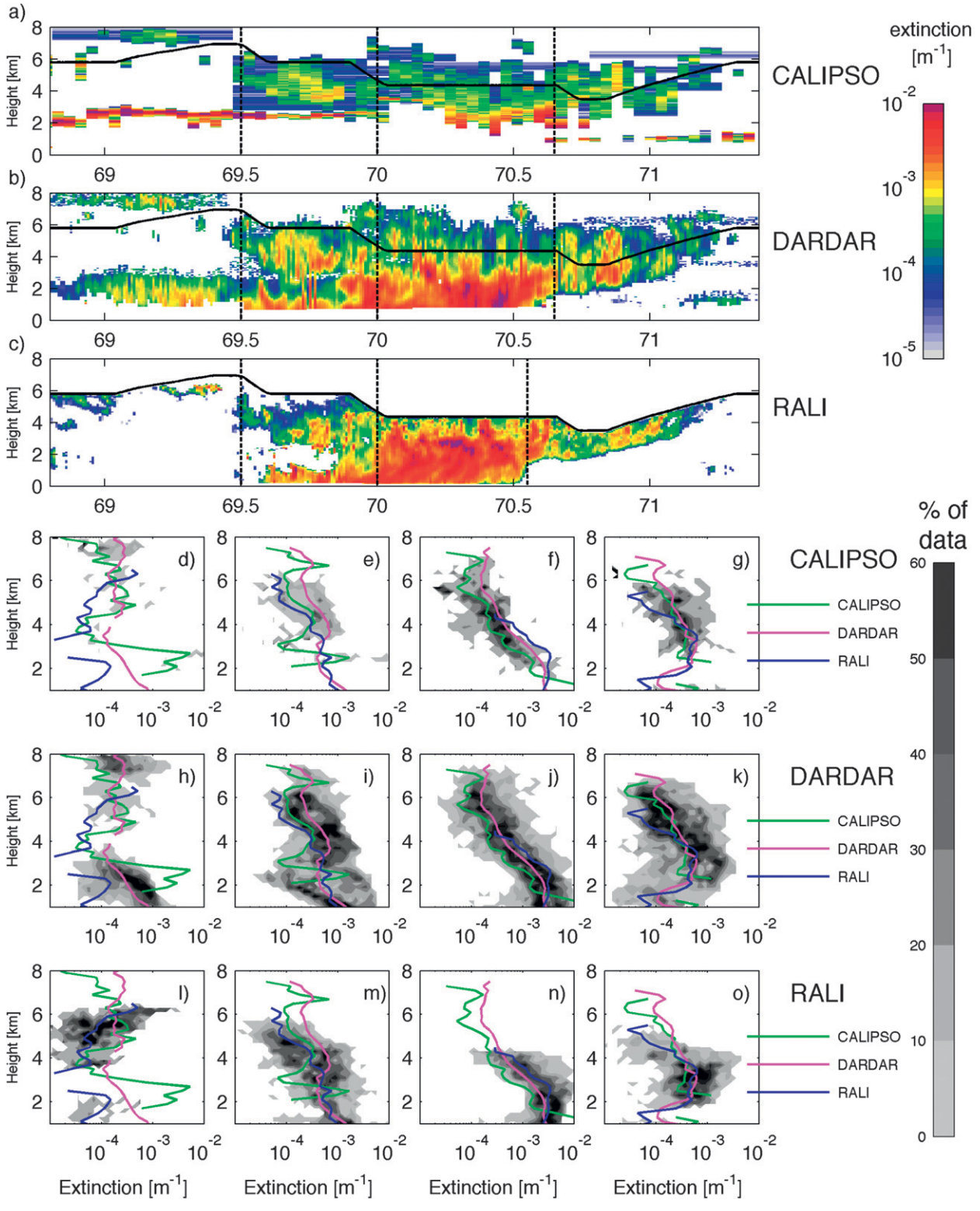

FIG. 10. As in Fig. 9, but for visible extinction. Only CALIOP, DARDAR, and RALI are represented as *CloudSat* cannot retrieve extinction. (a)–(c) The latitude height extinctions of CALIOP, DARDAR and RALI, respectively. For each region, the density distribution plots of extinction vs height and average values are shown for (d)–(g) CALIOP, (h)–(k) DARDAR, and (l)–(o) RALI.

the extinction-to-backscatter ratio is fixed. The Varcloud algorithm, used to derive the DARDAR product, accounts for multiple scattering using the model of Hogan (2006) and retrieves the extinction-to-backscatter ratio (the radar signal is used as an external constraint).

5. Conclusions and perspectives

The present paper aims to illustrate the considerable potential of RALI, the French airborne radar–lidar instrument, for studying cloud processes and evaluating satellite products when we have satellite overpasses. We have demonstrated the capability of this synergistic instrument to retrieve cloud properties and also to characterize the cloud phase at scales smaller than a kilometer, which is crucial for cloud process analysis. Due to their different wavelengths, radar and lidar instruments allow one to infer both cloud phase and cloud properties, as lidar signals are more sensitive to high concentrations of hydrometeors, while radar measurements are more sensitive to the size of the ice particles. We have adapted the variational approach described in Delanoë and Hogan (2008) to the airborne measurements to retrieve IWC, extinction, and effective radius. Note that, as was shown in Delanoë and Hogan (2008) for ground-based and satellite observations used by Delanoë and Hogan (2010), it is possible to retrieve cloud properties seamlessly where clouds are detected by both radar and lidar and where they are only sampled by one instrument. It has been highlighted that the combination of radar and lidar gives better results when compared to the in situ measurements and that in general radar overestimates IWC while lidar underestimates it.

The case of 1 April 2008 was chosen for its combination of thin and thick mixed-phase clouds and because of the availability of *CloudSat* and *CALIPSO* satellite overpass results and the presence of in situ measurements on board the aircraft. One common way to assess satellite cloud products is to compare the retrieved properties with collocated in situ measurements. However, as with others who have tried to do so, we encounter collocation and sampling issues, as mentioned in section 4. These issues can be partly overcome when aircraft remote sensing instruments are available to link the very fine scales (a few meters, characterized by in situ probes) with larger scales, typically 1 km for *CALIPSO* and *CloudSat* satellites. We show that for our case study, *CALIPSO* retrievals tend to underestimate IWC and *CloudSat* tends to overestimate IWC. The DARDAR product lies mostly between the *CALIPSO* and *CloudSat* values, as the instrument synergy allows for the retrieval of both small and large ice crystals. We also note that DARDAR and *CALIPSO* extinction retrievals give similar results.

Future field campaigns will ideally include IWC bulk measurements such as from Nevzorov (Korolev et al. 1998) or counterflow virtual impactor (CVI; Twohy et al. 1997) probes. It will then be possible to precisely evaluate the retrieved IWC from both aircraft and satellite measurements. We remain dependent on the choice of the mass–size relationship assumption, which is still a weakness of most of the known retrieval techniques. We are also working on assimilating Doppler velocity from the radar (Delanoë et al. 2007) and high spectral resolution capability, which should improve retrieval. During the POLARCAT campaign the Doppler measurement was available; unfortunately, however, due to the antenna configuration it could not be used in any of our microphysical retrievals. We need at least three antennas, pointing in three noncollinear directions, to isolate the terminal fall velocity from the vertical air motion. The high spectral resolution lidar, which was not available during POLARCAT, will also improve the extinction retrieval, as the extinction-to-backscatter ratio will not have to be assumed constant along the vertical.

The RALI platform will be perfectly designed to prepare and to evaluate the future EarthCare mission (ESA 2004). This satellite, to be launched in late 2015, will be flown with some key components of the A-Train constellation on the same platform. The mission aims to study cloud and aerosol impacts on the earth radiative budget, including a 95-GHz Doppler cloud radar, a high spectral resolution lidar at 355 nm, an infrared imager, and a broadband radiometer.

Acknowledgments. We thank the engineers and technicians who are continuously working on the LNG and RASTA projects at DT/INSU and LATMOS. Julien Delanoë's research is partly funded by CNES. Spaceborne data were provided by NASA/CNES and we thank the ICARE Data and Services Center (http://www.icare-lille1.fr) for providing access to the data used in this study. We would like to acknowledge POLARCAT-France, which received funding from ANR, CNES, CNRS-INSU, IPEV, and EUFAR. We would like to acknowledge the follow-on French project CLIMSLIP-LEFE.

REFERENCES

Austin, R. T., A. J. Heymsfield, and G. L. Stephens, 2009: Retrieval of ice cloud microphysical parameters using the CloudSat millimeter-wave radar and temperature. *J. Geophys. Res.,* **114,** D00A23, doi:10.1029/2008JD010049.

Bouniol, D., and Coauthors, 2010: Using continuous ground-based radar and lidar measurements for evaluating the representation of clouds in four operational models. *J. Appl. Meteor. Climatol.,* **49,** 1971–1991.

Brown, P. R. A., and P. N. Francis, 1995: Improved measurements of the ice water content in cirrus using a total-water probe. *J. Atmos. Oceanic Technol.,* **12,** 410–414.

de Boer, G., E. Eloranta, and M. Shupe, 2009: Arctic mixed-phase stratus properties from multiple years of surface-based measurements at two high-latitude locations. *J. Atmos. Sci.,* **66,** 2874–2887.

Delanoë, J., and R. J. Hogan, 2008: A variational scheme for retrieving ice cloud properties from combined radar, lidar and infrared radiometer. *J. Geophys. Res.,* **113,** D07204, doi:10.1029/2007JD009000.

——, and ——, 2010: Combined CloudSat-CALIPSO-MODIS retrievals of the properties of ice clouds. *J. Geophys. Res.,* **115,** D00H29, doi:10.1029/2009JD012346.

——, A. Protat, J. Testud, D. Bouniol, A. J. Heymsfield, A. Bansemer, P. R. A. Brown, and R. M. Forbes, 2005: Statistical properties of the normalized ice particle size distribution. *J. Geophys. Res.,* **110,** 10 201, doi:10.1029/2004JD005405.

——, ——, ——, ——, ——, ——, and ——, 2007: The characterization of ice clouds properties from Doppler radar measurements. *J. Appl. Meteor. Climatol.,* **46,** 1682–1698.

——, R. J. Hogan, R. M. Forbes, A. Bodas-Salcedo, and T. H. M. Stein, 2011: Evaluation of ice cloud representation in the ECMWF and UK Met Office models using CloudSat and CALIPSO data. *Quart. J. Roy. Meteor. Soc.,* **137B,** 2064–2078, doi:10.1002/qj.882.

Deng, M., G. G. Mace, Z. Wang, and H. Okamoto, 2010: Tropical Composition, Cloud and Climate Coupling Experiment validation for cirrus cloud profiling retrieval using CloudSat radar and CALIPSO lidar. *J. Geophys. Res.,* **115,** D00J15, doi:10.1029/2009JD013104.

Eloranta, E., T. Uttal, and M. Shupe, 2007: Cloud particle size measurements in arctic clouds using lidar and radar data. *Int. Geoscience and Remote Sensing Symp. (IGARSS),* Barcelona, Spain, IEEE, 2265–2267, doi:10.1109/IGARSS.2007.4423292.

ESA, 2004: Earthcare - Earth Clouds, Aerosols and Radiation Explorer. European Space Agency SP-1279(1), 60 pp.

Field, P. R., A. J. Heymsfield, and A. Bansemer, 2006: Shattering and particle interarrival times measured by optical array probes in ice clouds. *J. Atmos. Oceanic Technol.,* **23,** 1357–1371.

Francis, P. N., P. Hignett, and A. Macke, 1998: The retrieval of cirrus cloud properties from aircraft multi-spectral reflectance measurements during EUCREX'93. *Quart. J. Roy. Meteor. Soc.,* **124,** 1273–1291.

Gayet, J.-F., S. Asano, A. Yamazaki, A. Uchiyama, A. Sinyuk, O. Jourdan, and F. Auriol, 2002a: Two case studies of winter continental–type water and mixed-phase stractocumuli over the sea 1. Microphysical and optical properties. *J. Geophys. Res.,* **107,** 4569, doi:10.1029/2001JD001106.

——, and Coauthors, 2002b: Quantitative measurement of the microphysical and optical properties of cirrus clouds with four different in situ probes: Evidence of small ice crystals. *Geophys. Res. Lett.,* **29,** 2230, doi:10.1029/2001GL014342.

Heymsfield, A. J., 2007: On measurements of small ice particles in clouds. *Geophys. Res. Lett.,* **34,** L23812, doi:10.1029/2007GL030951.

——, D. Winker, and G. J. van Zadelhoff, 2005: Extinction-ice water content-effective radius algorithms for CALIPSO. *Geophys. Res. Lett.,* **32,** L10807, doi:10.1029/2005GL022742.

——, C. Schmitt, A. Bansemer, and C. H. Twohy, 2010: Improved representation of ice particle masses based on observations in natural clouds. *J. Atmos. Sci.,* **67,** 3303–3318.

Hogan, R. J., 2006: Fast approximate calculation of multiply scattered lidar returns. *Appl. Opt.,* **45,** 5984–5992.

Illingworth, A. J., and Coauthors, 2007: Cloudnet—Continuous evaluation of cloud profiles in seven operational models using ground-based observations. *Bull. Amer. Meteor. Soc.,* **88,** 883–898.

Intrieri, J. M., G. L. Stephens, W. L. Eberhart, and T. Uttal, 1993: A method for determining cirrus cloud particle sizes using lidar and radar backscatter techniques. *J. Appl. Meteor.,* **32,** 1074–1082.

——, M. D. Shupe, T. Uttal, and B. J. McCarty, 2002: An annual cycle of Arctic cloud characteristics observed by radar and lidar at SHEBA. *J. Geophys. Res.,* **107,** 8030, doi:10.1029/2000JC000423.

King, M. D., Tsay S.-C.Platnick S. E.Wang M., and K.-N. Liou, 1998: Cloud retrieval algorithms for modis: Optical thickness, effective particle radius, and thermodynamic phase. MODIS Algorithm Theoretical Basis Doc. ATBD-MOD-05, NASA GSFC, 79 pp.

Knollenberg, R. G., 1970: The optical array: An alternative to scattering or extinction for airborne particle size determination. *J. Appl. Meteor.,* **9,** 86–103.

Korolev, A., and G. A. Isaac, 2005: Shattering during sampling by OAPs and HVPs. Part I: Snow particles. *J. Atmos. Oceanic Technol.,* **22,** 528–542.

——, J. W. Strapp, G. A. Isaac, and A. N. Nevzorov, 1998: The Nevzorov airborne hot-wire LWC–TWC probe: Principle of operation and performance characteristics. *J. Atmos. Oceanic Technol.,* **15,** 1495–1510.

Lawson, R. P., and B. A. Baker, 2006: Improvement in determination of ice water content from two-dimensional particle imagery. Part II: Applications to collected data. *J. Appl. Meteor. Climatol.,* **45,** 1291–1303.

——, ——, C. G. Schmitt, and T. L. Jensen, 2001: An overview of microphysical properties of Arctic clouds observed in May and July 1998 during FIRE ACE. *J. Geophys. Res.,* **106,** 14 989–15 014.

Li, L., and Coauthors, 2001: Retrieval of atmospheric attenuation using combined ground-based and airborne 95-GHz cloud radar measurements. *J. Atmos. Oceanic Technol.,* **18,** 1345–1353.

Mace, G. G., Q. Zhang, M. Vaughn, R. Marchand, G. Stephens, C. Trepte, and D. Winker, 2009: A description of hydrometeor layer occurrence statistics derived from the first year of merged CloudSat and CALIPSO data. *J. Geophys. Res.,* 114, D00A26, doi:10.1029/2007JD009755.

Mioche, G., D. Josset, J.-F. Gayet, J. Pelon, A. Garnier, A. Minikin, and A. Schwarzenböck, 2010: Validation of the CALIPSO-CALIOP extinction coefficients from in situ observations in midlatitude cirrus clouds during the CIRCLE-2 experiment. *J. Geophys. Res.,* **115,** D00H25, doi:10.1029/2009JD012376.

Mitrescu, C., J. M. Haynes, G. L. Stephens, S. D. Miller, G. M. Heymsfield, and M. J. McGill, 2005: Cirrus cloud optical, microphysical, and radiative properties observed during the CRYSTAL-FACE experiment: A lidar-radar retrieval system. *J. Geophys. Res.,* **110,** D09208, doi:10.1029/2004JD005605.

Okamoto, H., S. Iwasaki, M. Yasui, H. Horie, H. Kuroiwa, and H. Kumagai, 2003: An algorithm for retrieval of cloud microphysics using 95-GHz cloud radar and lidar. *J. Geophys. Res.,* **108,** 4226–4247.

Protat, A., and Coauthors, 2004: Le projet RALI: Etude des nuages faiblement précipitants par télédétection active. *Meteorologie,* **47,** 23–33.

——, and Coauthors, 2009: Assessment of Cloudsat reflectivity measurements and ice cloud properties using ground-based and airborne cloud radar observations. *J. Atmos. Oceanic Technol.,* **26,** 1717–1741.

——, D. Bouniol, E. J. O'Connor, H. K. Baltink, J. Verlinde, and K. Widener, 2011a: *CloudSat* as a global radar calibrator. *J. Atmos. Oceanic Technol.,* **28,** 445–452.

——, G. McFarquhar, J. Um, and J. Delanoë, 2011b: Obtaining best estimates for the microphysical and radiative properties of tropical ice clouds from TWP-ICE in situ microphysical observations. *J. Appl. Meteor. Climatol.,* **50,** 895–915.

Rauber, R. M., and A. Tokay, 1991: An explanation for the existence of supercooled water at the top of cold clouds. *J. Atmos. Sci.,* **48,** 1005–1023.

Rodgers, C. D., 2000: *Inverse Methods for Atmospheric Sounding: Theory and Practice.* World Scientific, 238 pp.

Shupe, M., 2011: Clouds at Arctic atmospheric observatories. Part II: Thermodynamic phase characteristics. *J. Appl. Meteor. Climatol.,* **50,** 645–661.

——, and J. M. Intrieri, 2004: Cloud radiative forcing of the Arctic surface: The influence of cloud properties, surface albedo, and solar zenith angle. *J. Climate,* **17,** 616–628.

——, S. Y. Matrosov, and T. Uttal, 2006: Arctic mixed-phase cloud properties derived from surface-based sensors at SHEBA. *J. Atmos. Sci.,* **63,** 697–711.

——, V. Walden, E. Eloranta, T. Uttal, J. Campbell, S. Starkweather, and M. Shiobara, 2011: Clouds at Arctic atmospheric observatories. Part I: Occurrence and macrophysical properties. *J. Appl. Meteor. Climatol.,* **50,** 626–644.

Stein, T. M., J. Delanoë, and R. J. Hogan, 2011: A comparison between four different retrieval methods for ice cloud properties using data from *CloudSat*, *CALIPSO*, and MODIS. *J. Appl. Meteor. Climatol.,* **50,** 1952–1969.

Stephens, G. L., and Coauthors, 2002: The Cloudsat Mission and the A-Train. *Bull. Amer. Meteor. Soc.,* **83,** 1771–1790.

Strapp, J. W., F. Albers, A. Reuter, A. V. Korolev, U. Maixner, E. Rashke, and Z. Vukovic, 2001: Laboratory measurements of the response of a PMS OAP-2DC. *J. Atmos. Oceanic Technol.,* **18,** 1150–1170.

Tanelli, S., S. L. Durden, E. Im, K. S. Pak, D. G. Reinke, P. Partain, J. M. Haynes, and R. T. Marchand, 2008: Cloudsat's cloud profiling radar after 2 years in orbit: Performance, external calibration, and processing. *IEEE Trans. Geosci. Remote Sens.,* **46,** 3560–3573.

Tinel, C., J. Testud, R. J. Hogan, A. Protat, J. Delanoë, and D. Bouniol, 2005: The retrieval of ice cloud properties from cloud radar and lidar synergy. *J. Appl. Meteor.,* **44,** 860–875.

Twohy, C. H., A. J. Schanot, and W. A. Cooper, 1997: Measurements of condensed water content in liquid and ice clouds using an airborne counterflow virtual impactor. *J. Atmos. Oceanic Technol.,* **14,** 197–202.

Waliser, D. E., and Coauthors, 2009: Cloud ice: A climate model challenge with signs and expectations of progress. *J. Geophys. Res.,* **114,** D00A21, doi:10.1029/2008JD010015.

Wang, Z., and K. Sassen, 2002: Cirrus cloud microphysical property retrieval using lidar and radar measurements. Part I: Algorithm description and comparison with in situ data. *J. Appl. Meteor.,* **41,** 218–229.

Winker, D. M., J. Pelon, and M. P. McCormick, 2003: The CALIPSO mission: Spaceborne lidar for observation of aerosols and clouds. *Lidar Remote Sensing for Industry and Environment Monitoring III,* U. N. Singh, T. Itabe, and Z. Liu, Eds., International Society for Optical Engineering (SPIE Proceedings, Vol. 4893), 1–11.

Yoshida, R., H. Okamoto, Y. Hagihara, and H. Ishimoto, 2010: Global analysis of cloud phase and ice crystal orientation from Cloud-Aerosol Lidar and Infrared Pathfinder Satellite Observation (CALIPSO) data using attenuated backscattering and depolarization ratio. *J. Geophys. Res.,* **115,** D00H32, doi:10.1029/2009JD012334.

Young, S. A., and M. A. Vaughan, 2009: The retrieval of profiles of particulate extinction from Cloud-Aerosol Lidar and Infrared Pathfinder Satellite Observation (CALIPSO) data: Algorithm description. *J. Atmos. Oceanic Technol.,* **26,** 1105–1119.